**SANDIA REPORT**
SAND2000-8599
Unlimited Release
Printed April 2000

# Experimental Measurements of the Thermal Conductivity of Ash Deposits: Part 1. Measurement Technique

(To be submitted to *Energy and Fuels*)

A. L. Robinson, S. G. Buckley, N. Yang, L. L. Baxter

Prepared by
Sandia National Laboratories
Albuquerque, New Mexico 87185 and Livermore, California 94550

Sandia is a multiprogram laboratory operated by Sandia Corporation, a Lockheed Martin Company, for the United States Department of Energy under Contract DE-AC04-94AL85000.



Sandia National Laboratories

Issued by Sandia National Laboratories, operated for the United States Department of Energy by Sandia Corporation.



Available to DOE and DOE contractors from
Office of Scientific and Technical Information
P.O. Box 62
Oak Ridge, TN 37831

Prices available from (703) 605-6000
Web site: http://www.ntis.gov/ordering.htm

Available to the public from
National Technical Information Service
U.S. Department of Commerce
5285 Port Royal Rd
Springfield, VA 22161

NTIS price codes
Printed copy: A03
Microfiche copy: A01

## DISCLAIMER

Portions of this document may be illegible in electronic image products. Images are produced from the best available original document.

SAND2000-8599
Unlimited Release
Printed April 2000

# Experimental Measurements of the Thermal Conductivity of Ash Deposits: Part 1. Measurement Technique

Allen L. Robinson*, Steven G. Buckley†, Larry L. Baxter
Combustion Research Facility
Sandia National Laboratories
Livermore, CA 94551-0969

## Abstract

This paper describes a technique developed to make *in situ*, time-resolved measurements of the effective thermal conductivity of ash deposits formed under conditions that closely replicate those found in the convective pass of a commercial boiler. Since ash deposit thermal conductivity is thought to be strongly dependent on deposit microstructure, the technique is designed to minimize the disturbance of the natural deposit microstructure. Traditional techniques for measuring deposit thermal conductivity generally do not preserve the sample microstructure. Experiments are described that demonstrate the technique, quantify experimental uncertainty, and determine the thermal conductivity of highly porous, unsintered deposits. The average measured thermal conductivity of loose, unsintered deposits is $0.14 \pm 0.03$ W/(m K), approximately midway between rational theoretical limits for deposit thermal conductivity.

* Corresponding author. Currently at the Dept. of Mechanical Engineering and the Dept. of Engineering and Public Policy, Carnegie Mellon University, Pittsburgh, PA 15213

† Currently at the Department of Mechanical Engineering, 2181 Glenn L. Martin Building, University of Maryland, College Park, MD 20742

This page intentionally left blank

## Introduction

Ash deposition frequently plays a dominant role in the design and operation of power generation systems that operate on coal, biomass, black liquor and other ash-forming fuels[1]. Ash deposits form from fly ash, inorganic vapors, and some gas species that deposit or react through a variety of mechanisms[2]. One effect of ash deposits is to reduce heat transfer rates to furnace walls, superheater tubes, and other heat transfer surfaces[3,4]. The magnitude of this reduction largely depends on the thickness, thermal conductivity, and emissivity of the deposits. This paper discusses the effective thermal conductivity of ash deposits; several reviews have been written on this subject[3,5].

Heat transfer through an ash deposit occurs by conduction through both the solid and gas phases and radiation through the transparent phases. Therefore, the effective thermal conductivity, a lumped parameter, which accounts for heat transfer by all these modes, is used to characterize the heat transfer rate through a deposit. The phrase "thermal conductivity" refers to the effective thermal conductivity of the deposit.

Several investigations report measurements of the thermal conductivity of ash deposits or ash-deposit-like material[3,6-13]. The reported values span several orders of magnitude from 0.012 W/(m K)[9] to 15 W/(m K)[3]. Two investigations[8,9] report thermal conductivity values less than that of air, suggesting noncontinuum heat conduction in which the mean free path of a gas molecule exceeds the characteristic pore dimension of the deposit. At the other extreme, several investigators report effective thermal conductivities that exceed those of the non-porous solid material from which deposits are typically composed[3].

The thermal conductivity of ash deposits is believed to depend primarily on the deposit physical structure or microstructure[3,14]. For example, the denser, more-interconnected the deposit structure, the higher its thermal conductivity. Highly porous deposits of loose, unsintered, particulate matter generally have low values of thermal conductivity, potentially approaching that of air, ~ 0.06 W/(m K) at typical deposit temperatures. Solid, sintered deposits have high values of thermal conductivity, approaching that of the solid phase of the deposit (3 W/(m K) for deposits consisting primarily of silica-based material).

Composition, particle size, and temperature have also been shown to influence deposit thermal conductivity; however, the published results are not consistent on these issues[3]. These inconsistencies are not surprising considering that these parameters can both directly and indirectly influence deposit thermal conductivity. For example, the chemical composition determines the underlying thermophysical properties of the deposit materials. However, a potentially more important influence of chemical composition may be indirect through its effect on sintering propensity. Changes in deposit microstructure due to sintering are likely to be more important than variation in the thermophysical properties of the underlying deposit materials.

The importance of deposit microstructure in determining the effect of ash deposits on heat transfer rates raises concerns regarding previously reported measurements of ash deposit thermal conductivity. The majority of the reported thermal conductivity measurements are based on *post mortem* analysis techniques that destroy or significantly alter the physical structure of a deposit. Typically, powdered or pelletized ash samples are examined, which are generated using a laboratory ashing furnace, captured fly ash from a power plant, or a pulverized deposit from a boiler. These samples have chemical compositions similar to actual boiler deposits, but not the same microstructure. A few investigations have examined hybrid samples of intact, sintered deposits, and fly ash used to fill in gaps between the irregular-shaped deposit and the surfaces of the measurement device[7,9]. Based on their analysis of these hybrid samples, Anderson et al.[7] concluded that "crushing samples of porous coal ash deposits can significantly bias effective thermal conductivities." To address this issue, we have developed a novel technique that allows direct examination of the thermal conductivity of actual deposits, avoiding the problems of the previous *post mortem* analyses.

In this two-part study, we report an experimental investigation into the thermal conductivity of ash deposits. In this paper, we describe a novel experimental technique to measure the thermal conductivity of ash deposits *in situ* as they form in a pilot-scale combustor. We present measurements of thermal conductivity of deposits formed while firing Illinois #6 coal and wheat straw and quantify the experimental uncertainty. In the second part of this study[15], we use this technique to examine the impacts of sintering and changes in deposit microstructure on deposit thermal conductivity. Preliminary measurements and a partial description of the experimental technique have been previously reported[12].

## Experimental Methods

Most previous investigations of ash deposit thermal conductivity examine highly disturbed, deposit-like materials (fly ash, fuel ash, or crushed boiler deposits) in a well-characterized environment. The approach described below is guided by the hypothesis that ash deposit thermal conductivity is largely determined by deposit microstructure. Consequently, thermal conductivity measurements must be made in such a way as to minimize the disturbance of the natural deposit microstructure. To achieve this objective, we have designed a novel experiment to measure deposit thermal conductivity *in situ,* as the deposit forms, in a pilot-scale combustor.

### Experimental facility

Experiments to measure the thermal conductivity of fly ash deposits were conducted using the Multifuel Combustor (MFC) at Sandia National Laboratories. A schematic diagram of the MFC is shown in Figure 1. The MFC is a pilot-scale (~ 30 kW), 4.2-m-high, down-fired, turbulent flow combustor that simulates gas temperature, gas composition, and residence times experienced by particles in entrained flow combustion systems such as pulverized-coal-fired boilers. The reactor has a 15-cm-diameter SiC reactor tube, and consists of seven 0.6-m-tall modular sections. Electrical heaters allow wall temperatures of the top six sections to follow a prescribed pattern determined by independent controllers. A more detailed discussion of the MFC is available in the literature[16].

The reactor tube leads to the open test section of the MFC where deposits are collected and analyzed using a variety of instruments (see Figure 1). Figure 2 shows an illustration of the configuration of the test section for the thermal conductivity experiments. The major features of this equipment are discussed in the following sections.

### Experimental Procedure

A 65/35% (by mass) blend of Illinois #6 coal and wheat straw was fired in the MFC to generate an ash deposit. Utility-grind, pulverized coal (70% through a 200 mesh) was prepared separately from the wheat straw. Samples of wheat straw were ground to pass through a 0.5-mm mesh. The straw-coal blend formed part of a series of experiments examining the effects of biomass-coal cofiring on fireside combustion processes[17]. Results from standard fuel analyses are listed in the second part of this study[15].

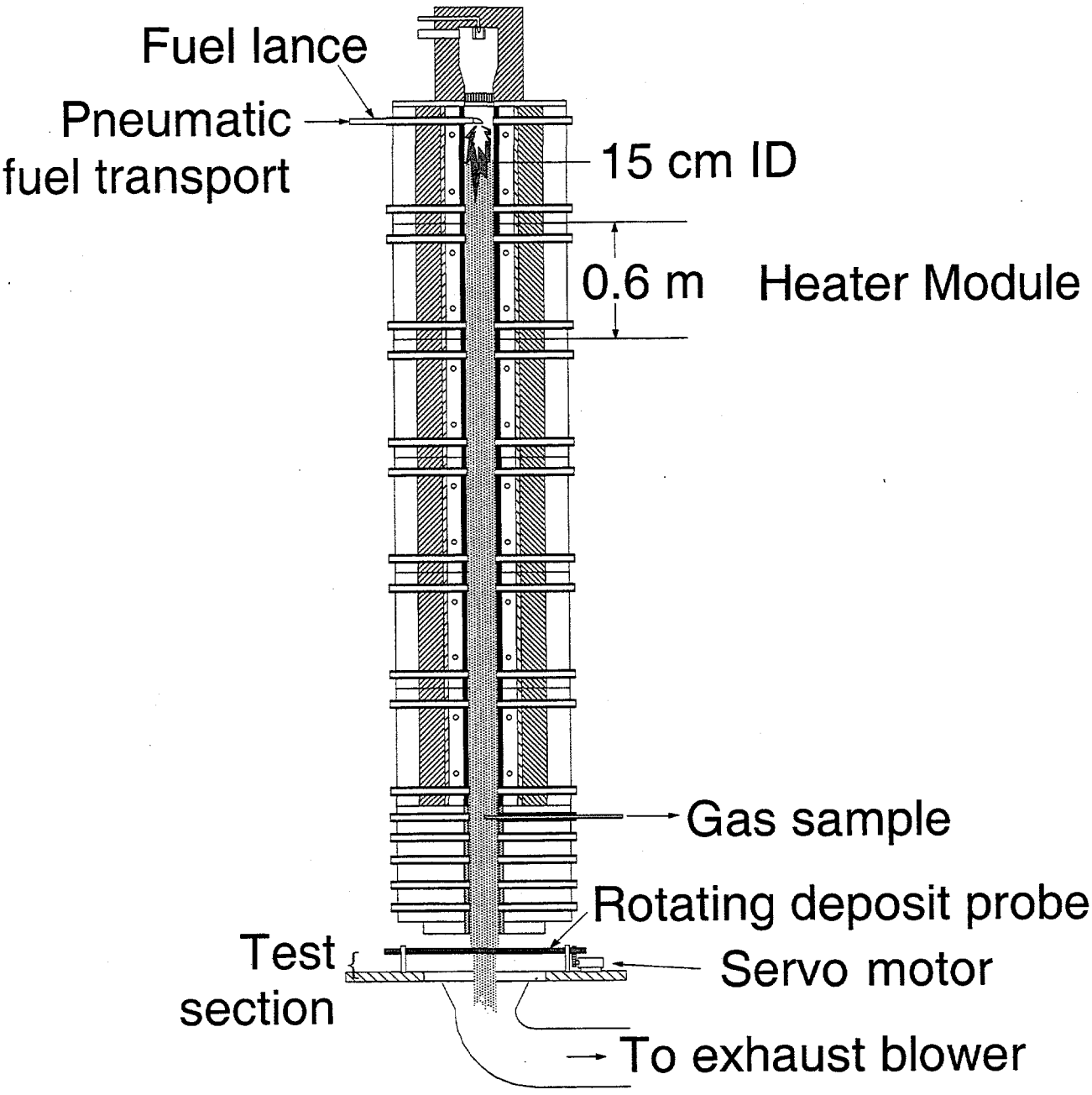


Figure 1 Schematic diagram of the Multifuel Combustor.

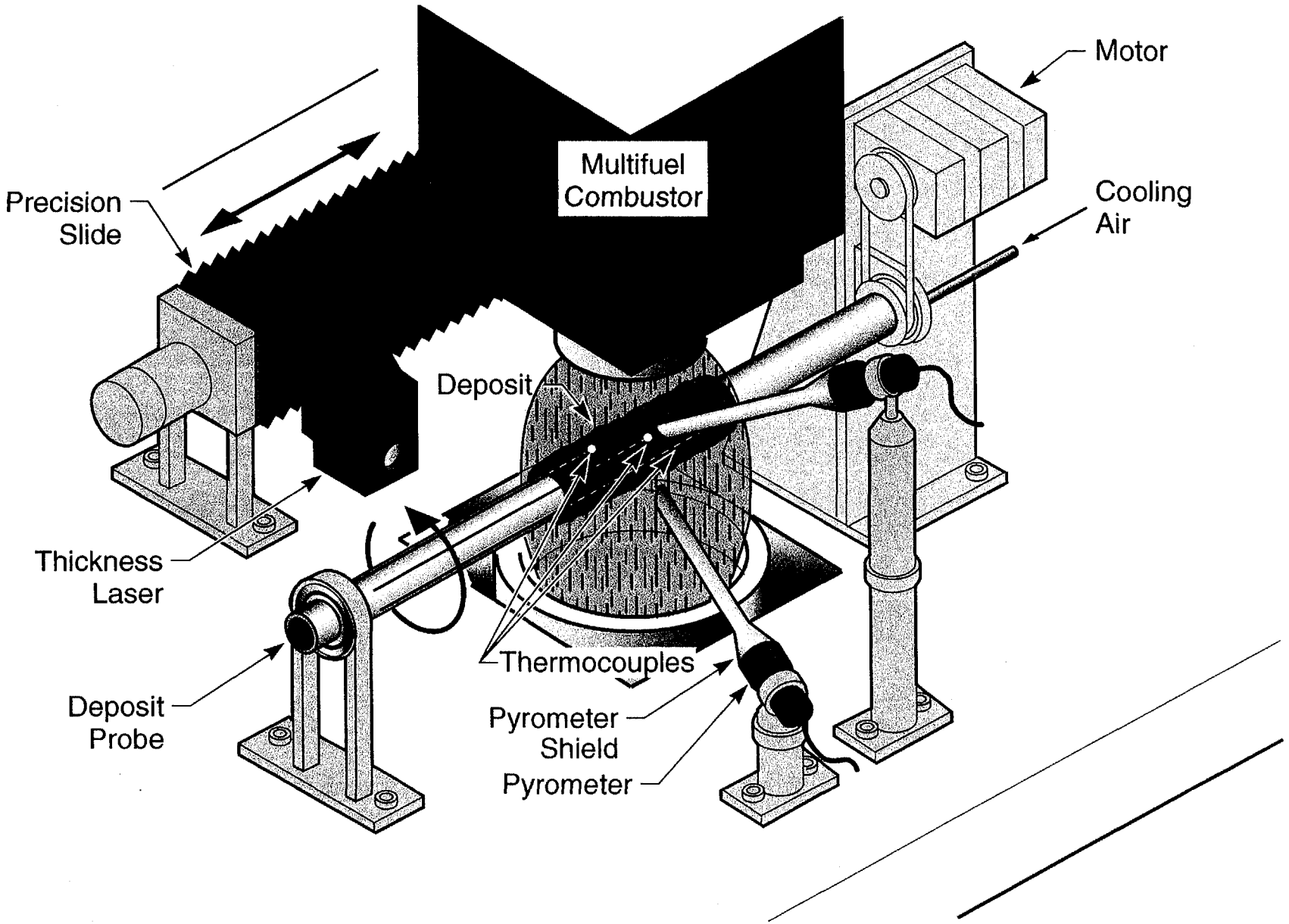


Figure 2 Illustration of the experimental set-up in the test section of the Multifuel Combustor. This figure is not drawn precisely to-scale, but provides a reasonable representation of the probes and instrumentation used for these experiments.

Solid fuel enters the MFC pneumatically at the top of the reactor just below the natural gas burner (see Figure 1). Under the conditions of these experiments, the residence time of a fuel particle in the combustor was approximately 1 sec, which is comparable to the residence time in commercial boilers. The fuel feed rate was set to maintain an oxygen concentration of 4% by volume (dry basis) in the combustion products at the exit of the reactor, which corresponds to the standard utility practice of firing with 20% excess air. The natural gas burner was not operated for the experiments described in this paper.

Ash deposits are collected on an instrumented, air-cooled, stainless steel probe placed in the test section of the MFC (see Figures 1 and 2). Although an ash deposit is formed over an approximately 15-cm section of the deposition probe, for thermal conductivity analysis we only examine the center 3.5 cm of the deposit, which we refer to as the deposit test section. Deposits are collected at relatively low probe temperatures (300 - 400°C) to create a loose, unsintered, particulate deposit. The average temperature of the combustion products flowing past the probe was ~ 950°C. A constant cooling air-flow rate through the probe was maintained to simulate steam flows in convection-pass tubes in utility boilers.

The gas and particle velocities through the test section of the MFC are roughly a factor of 4 smaller than typical convective pass velocities (~ 5 m/s in the MFC versus ~ 20 m/s in a power plant). Therefore, we cannot match both the Reynolds and Stokes numbers found in typical boilers. For these experiments, we choose to match the Stokes number found in typical boilers by selecting a probe with an appropriate outside diameter (2.2 cm). Deposit formation in coal-fired power plants is dominated by inertial impaction, which is a function of Stokes number. Matching Stokes numbers ensures that the size distribution of fly ash particles striking the deposition probe in the MFC is the same as the size distribution of particles hitting a superheater tube. The resulting ash deposits should have a physical structure and chemical composition similar to deposits formed in commercial coal-fired power plants. The Reynolds number of the deposition probe used in this study is roughly a factor of 10 smaller than that of a typical superheater tube, which results in lower convective heat transfer to the deposition probe in the MFC compared to a typical superheater tube. In all cases, we match the surface temperature of the deposition probe to that found in a utility boiler by adjusting the cooling air flow rate through the probe.

We rotate the deposition probe at a speed of 0.25 rpm to create a uniform, one-dimensional ash deposit. The slow rotation of the deposition probe does not measurably affect the fluid and particle flow around the probe because the rotational velocity is four orders of magnitude smaller than the velocity of the particles striking the probe surface. Therefore, we assume that the rotating the probe does not affect particle deposition and the resulting deposit microstructure. However, probe rotation does affect overall deposit shape (by design) and causes a significant periodic oscillation in the local deposit and probe temperature, as discussed later.

We use the deposit solid fraction to characterize the deposit density. For this analysis we measure the deposit mass at the end of an experiment. Combining this mass with the measured deposit volume (determined from the deposit thickness scans), we estimate the deposit bulk density. Assuming a density of 2.2 g $cm^{-3}$ for the solid material within the deposit, we convert the bulk density to solid fraction.

## Instrumentation

The experiment is designed to measure as many parameters as is possible directly, relying on analysis to combine these measurements to determine the thermal conductivity. Direct measurements include probe surface temperature, deposit thickness, deposit surface temperature, cooling air flow rate, and cooling air temperature change. These measurements are made *in situ* while the deposit forms on the deposition probe.

Probe surface temperature is measured using four type-K thermocouples embedded in the outside of the probe wall. These thermocouples are embedded 90° apart and distributed axially along the probe test section to monitor both the azimuthal and axial variation in the probe surface temperature. We assume that temperatures at the deposit-probe interface are equal to the measured probe surface temperature.

The thickness of the deposit is measured using a range-finding laser (Selcom, Model 2207-32/180-B) mounted on a precision, position-encoded bearing. The laser scans horizontally along the probe axis. Comparing results of successive scans along the same line of sight or face of the probe, we determine the thickness and growth rate of the deposit.

Three optical pyrometers (Accufiber, Model 100C) monitor the surface temperature of the deposit. In the baseline configuration, the pyrometers are focused at the center of the deposit test section, 70°, 110°, and 170° below the flow stagnation point. The pyrometer focal area is

approximately 1 $mm^2$. Periodically we change the orientation of the pyrometer to monitor surface temperatures at different locations. The pyrometers detect emitted, scattered, and reflected radiation along their line of sight. Radiation scattered and emitted by particles and radiation reflected by the deposit surface interferes with the surface temperature measurements. Shields which extend from the pyrometer lens to within ~ 4 mm of the surface of the deposit prevent particulate matter and nearly all of the scattered and reflected radiation from passing through the pyrometer line of sight. Radiation emitted by the MFC walls and from the flame ball in the combustor that is reflected by the top-half of the deposition probe (top 180°) can also significantly impact the measurements made using pyrometers. We correct for this reflected radiation by periodically rapidly shading the probe surface, and analyze the high-frequency response of the pyrometer signal to separate the reflected and emitted components of the radiation before the deposit surface cools significantly.

We use a laser pyrometer to determine the spectral emissivity of the bare probe at the beginning of each experiment and of the deposit surface at the end of each experiment. The deposit emissivity measurement is made *post mortem* immediately after removing the deposition probe from the combustor test section, before the temperature of the deposition probe has decreased by more than 100°C.

The radial heat flow through the deposit is determined using measurements of the cooling air flow rate and the cooling air temperature change across the deposit test section. The cooling air temperature change is measured using two type-K thermocouples mounted along the centerline inside the deposition probe. The thermocouples are mounted 3.5 cm apart at the outside edges of the probe test section. To prevent radial gas temperature gradients from biasing the measurements, the inside surface of the probe is rifled and screens are mounted immediately upstream of each thermocouple.

## Data Interpretation

The analysis to determine deposit thermal conductivity assumes that the deposit is a cylindrical shell of uniform thickness that is defined by the outside diameter of the deposit probe and the average measured deposit thickness. Assuming steady-state, two-dimensional heat transfer through the deposit and uniform deposit thermal conductivity, the deposit temperature distribution is described by,

$$\frac{\partial}{\partial r}\left(r\frac{\partial T}{\partial r}\right)+\frac{1}{r}\frac{\partial^2 T}{\partial \theta^2}=0 \qquad (1)$$

Using Equation (1), we numerically solve for the temperature distribution within the deposit using the measured azimuthal temperature distribution on the inside and outside surface of the deposit as boundary conditions. We then calculate the average temperature gradient at the inside edge of the deposit,

$$\overline{dT}=\frac{1}{2\pi}\int_0^{2\pi}\left.\frac{\partial T}{\partial r}\right|_{in}(\theta)d\theta \qquad (2)$$

Combining the result from Equation (2) and the measured heat transfer rate through the deposit Q, we obtain the effective thermal conductivity of the deposit,

$$k_{eff}=\frac{Q}{2\pi r_{in} L\overline{dT}}. \qquad (3)$$

where $2\pi r_{in} L$ is the area of the inside surface of the deposit ($r_{in}$ is the radius of the inside surface of the deposit, 1.1 cm, and L is the length of the probe test section, 3.5 cm).

## Results and Discussion

In this section, we examine data from an experiment conducted while firing a blend of Illinois #6 and wheat straw. The purpose is to thoroughly present and discuss the experimental technique and to quantify the experimental uncertainty. We first describe time-resolved measurements of the various parameters required to evaluate the thermal conductivity of an ash deposit – deposit thickness, deposit and probe surface temperature, and heat flux. These measurements are then combined to determine the thermal conductivity of the deposit. Finally, we discuss the magnitude and sources of uncertainty of the measurements.

### Surface temperature, deposit thickness, and heat flux measurements

Time-resolved measurements of deposit thickness, average deposit surface temperature, average probe surface temperature, and heat flux through the deposit are shown in Figure 3. The results indicate that a 5-mm-thick deposit formed over the course of this 2-hr experiment (Figure 3a) which created a 200°C average temperature difference between the deposit and probe surface (Figure 3b), and reduced the heat transfer through the deposit by 22% (Figure 3c). The results shown in Figure 3 are based on analyses of the data collected by the range-finding laser, optical pyrometers, and probe

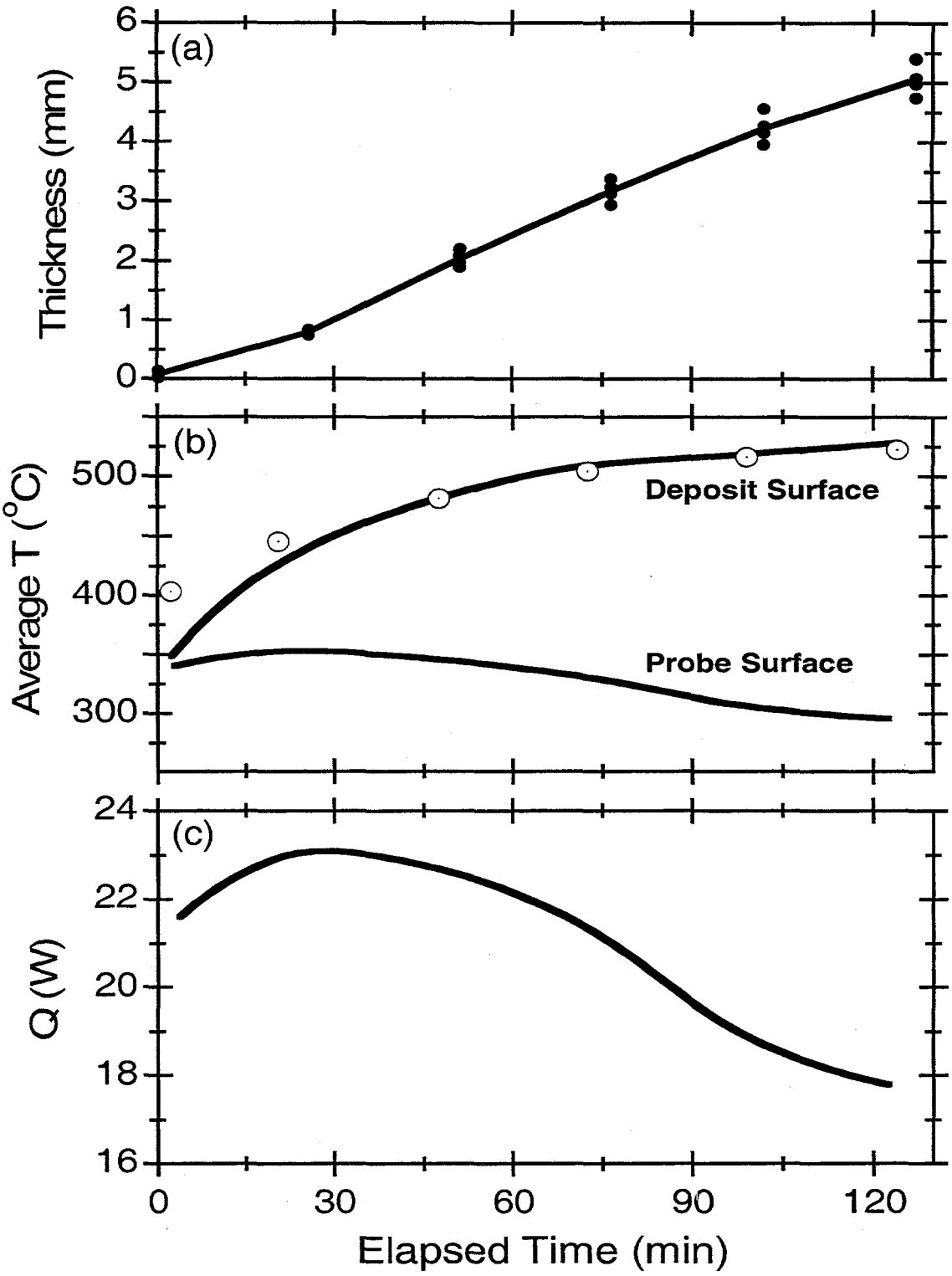


Figure 3 Time-resolved measurements: a) average deposit thickness, b) average probe and deposit surface temperatures, and c) heat transfer rate through the test section. The open circles in (c) represent the uncorrected deposit surface temperature, as described in the text.

thermocouples. We briefly describe these data and analyses before discussing the deposit thermal conductivity measurements.

**Deposit thickness**

Figure 3a presents results from the deposit thickness measurements. The symbols indicate the average deposit thickness for a given scan. The range-finding laser makes a set of 4 such scans each separated by 90°, every 25 minutes. The small variation (< 5% of the average) within a set of 4 thickness scans indicates the formation of a uniformly thick deposit around the probe. The average of each set of scans, indicated by the solid line, defines the thickness of the cylindrical shell used for the analysis of deposit thermal conductivity.

The thickness results shown in Figure 3a are determined through analysis of the range-finding laser scans such as those shown in Figure 4. These scans were all taken with the same probe orientation to illustrate deposit growth along one line of sight. The range-finding laser does not directly measure deposit thickness, but rather measures the distance between the laser and the deposit surface as a function of an axial position along the probe. We must subtract a baseline, which represents the location of the probe surface, from each laser scan to determine the deposit thickness. We have already subtracted this baseline from the results shown in Figure 4. To determine this baseline, we remove some of the deposit from the outside edges of the deposition zone. To clearly define the location of the probe surface, we fit a straight line to the measured probe surface location on each side of the deposit. This procedure does not disturb the thermal conductivity measurements because the deposit test section is only the center 3.5 cm of the approximately 15-cm wide deposition zone. This technique eliminates the errors caused by thermal deformation of the probe during the experiment.

The large variations in deposit thickness are caused by actual deposit surface roughness, not measurement uncertainty. These variations, up to 2 mm, are significantly larger than the measurement uncertainty of ± 40 μm. The measurement uncertainty is indicated by the variation in the line labeled 0 min in Figure 4.

**Deposit and probe surface temperature**

Figure 3b plots the average deposit and probe surface temperatures. The probe surface temperature is the average of the measurements of the 4 embedded thermocouples. The average deposit surface temperature is determined from the measurements of the 3 optical pyrometers, as

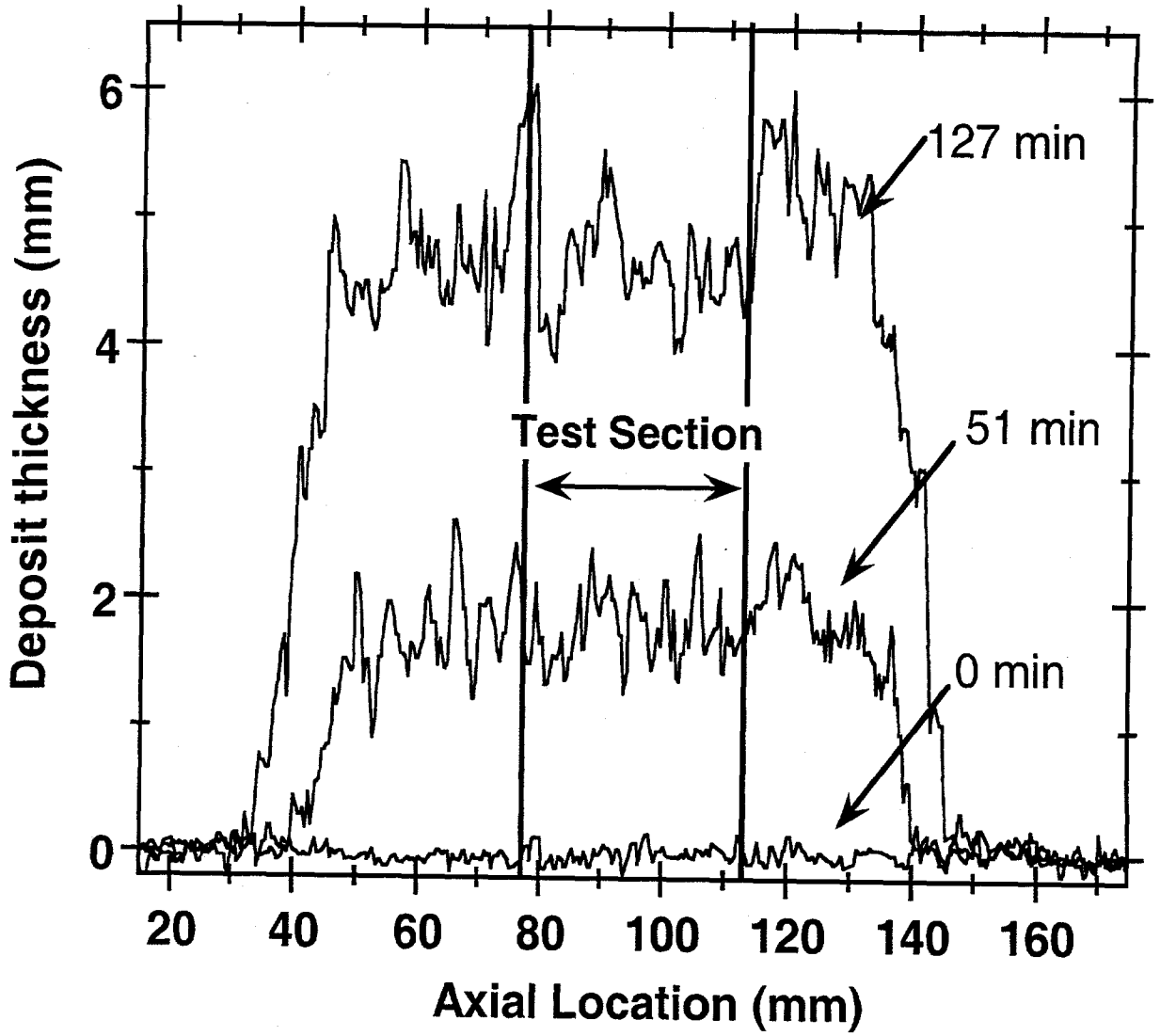


Figure 4 Deposit thickness measurements made with the range-finding laser system. As described in the text, the baseline representing the probe surface has been subtracted off these measurements. The labels indicate the elapsed experimental time when the scan was taken. For visual clarity, results from only three scans taken along the same probe orientation are shown. The axial location is determined by the position-encoded bearing and does not correspond to the distance across the reactor.

discussed below. As expected, the average temperature measured by the pyrometer agrees (within experimental uncertainty) with the average probe surface temperature measured with the thermocouples at the beginning of the experiment (before deposit formation). This agreement is an

important validation of the consistency of the different measurement techniques used to determine deposit thermal conductivity. As the deposit grows, the deposit surface temperature increases, while the probe surface temperature decreases. The constant cooling airflow rate in combination with the insulating effect of the deposit causes the large decline in the probe surface temperature.

Determination of the deposit surface temperature from the pyrometer data requires accounting for changes in deposit emissivity and correcting for radiation reflected by the deposit surface. To illustrate the magnitude of these corrections, the open circles in Figure 3b are the average deposit surface temperature calculated from the uncorrected pyrometer data (ignoring reflected radiation and assuming a deposit emissivity of 1). Comparing the uncorrected temperatures to our best estimate of the actual deposit surface temperature indicates that the corrections for emissivity and reflected radiation are significant (> 50°C) at the beginning of the experiment, but become negligible as the surface temperature of the deposit increases when the deposit grows. Therefore, these corrections have little impact on the measurements of deposit thermal conductivity.

Changes in the deposit emissivity have little effect on the thermal conductivity measurements. The laser pyrometer indicates that the surface emissivity varies between 0.9, the measured emissivity of the oxidized surface of the deposition probe, and 0.75, the measured deposit surface emissivity at the end of the experiment—a value consistent with previously reported measurements of deposit emissivity[3]. Over this range of values, the temperature calculated from the pyrometer data is relatively insensitive to deposit emissivity. For example, changing the deposit emissivity from 0.8 to 0.7 increases the deposit surface temperatures shown in Figure 3b by a maximum of 6°C; a small change compared to the 200°C temperature difference that commonly exists across a deposit.

Accounting for radiation reflected by the top-half (top 180°) of the deposit causes the majority of the correction in deposit surface temperature shown in Figure 3b. This correction is significant at the early stages of the experiment when the deposit surface temperature is relatively low. As the deposit grows which causes its surface temperature to increase, the magnitude of this correction approaches zero, becoming negligible above 550°C, because the magnitude of the reflected radiation is relatively constant but the intensity of the radiation emitted by the deposit rapidly increases with temperature.

A ten-minute period of surface temperature data is shown in Figure 5 to illustrate how we determine the azimuthal temperature distribution of the deposit and probe surface. These

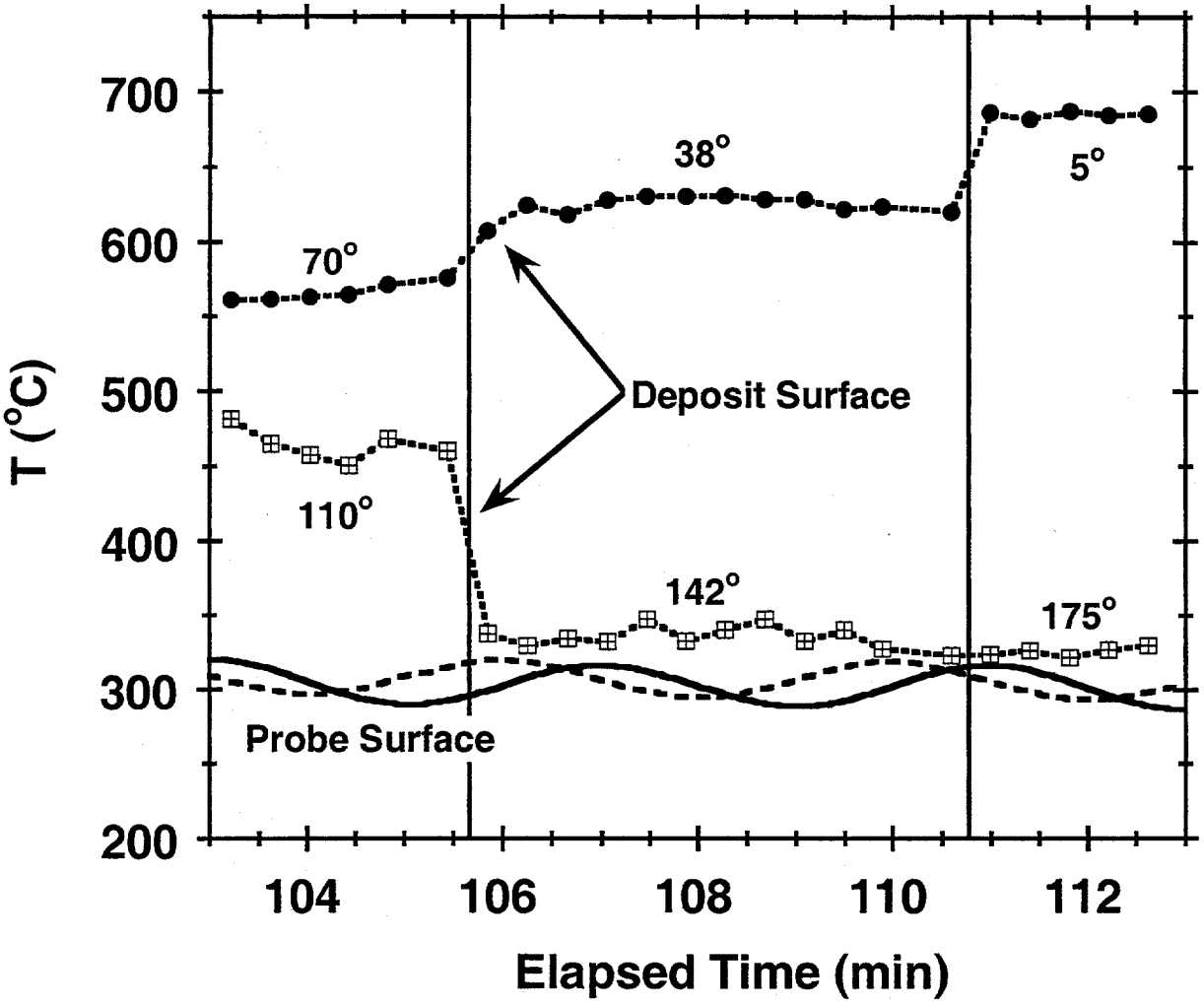


Figure 5 Ten minutes of probe and deposit surface temperature measurements. The numbers on the figure indicate the angle between the pyrometer focal volume and the leading edge of the probe. The vertical lines indicate approximately when the shifts in pyrometer orientation occurred. The pyrometer data have been corrected for deposit emissivity and reflected radiation. For visual clarity, measurements from two of the four probe surface temperature thermocouples and one of the three optical pyrometers are not shown.

temperature distributions are used as the boundary condition for the evaluation of equation (1). The embedded thermocouples measure the probe surface temperature at a fixed location on the rotating probe surface. Because the probe rotates, each thermocouple records a sinusoidal temperature oscillation with a period of 4 min. The 1-min phase leg between thermocouple signals is due to the azimuthal distribution of the thermocouples. The pyrometers measure the deposit surface

temperature at a fixed location in laboratory coordinates. We periodically reposition the pyrometers to measure the deposit surface temperature at different angular orientations. During the 10-min period shown in Figure 5 each pyrometer was repositioned twice. For example, one pyrometer was initially focused on a location 70° below the probe leading edge. This pyrometer was then repositioned to 38° and 5° below the leading edge, at 106 and 111 minutes elapsed time, respectively. We have corrected the pyrometer data shown in Figure 5 for deposit emissivity and reflected radiation.

Figure 6 plots the azimuthal distributions derived from the data shown in Figure 5. The peak temperature occurs at the leading edge of the probe, 0°. We align and average the signals from each thermocouple to determine the average probe surface temperature as a function of $\theta$. We fit, using least squares, a sinusoid to the optical pyrometer data to determine the deposit surface temperature distribution. The open circles shown in Figure 6 represent the average deposit surface temperature measured at 8 different angular orientations using the three different optical pyrometers for the 10-min period shown in Figure 5. We use a sinusoid to estimate the deposit surface temperature profile because a sinusoid very accurately represents the azimuthal variation in the measurements and is consistent with theoretical analysis[18]. The large amplitude of the sinusoid describing the deposit surface temperature is caused by the low thermal conductivity of the deposit relative to the stainless steel probe.

**Heat flux**

Data shown in Figure 3c indicate that the deposit decreased the heat transfer to the cooling air by 22% (relative to the peak heat transfer rate). The heat flux increases during the first 30 minutes of the experiment, because of the change in the thermal load in the MFC that occurs at the beginning of an experiment when the solid fuel feeder is turned on. Measurements of the MFC exit gas temperature indicates that the MFC reaches thermal equilibrium in approximately 30 minutes after the turning on the solid fuel feeder.

## Deposit Thermal Conductivity

Time-resolved measurements of the thermal conductivity from three different experiments are shown in Figure 7. The open circles labeled Expt. 2 represent the thermal conductivity measurements corresponding to the data presented in Figures 3-6. Results from two additional

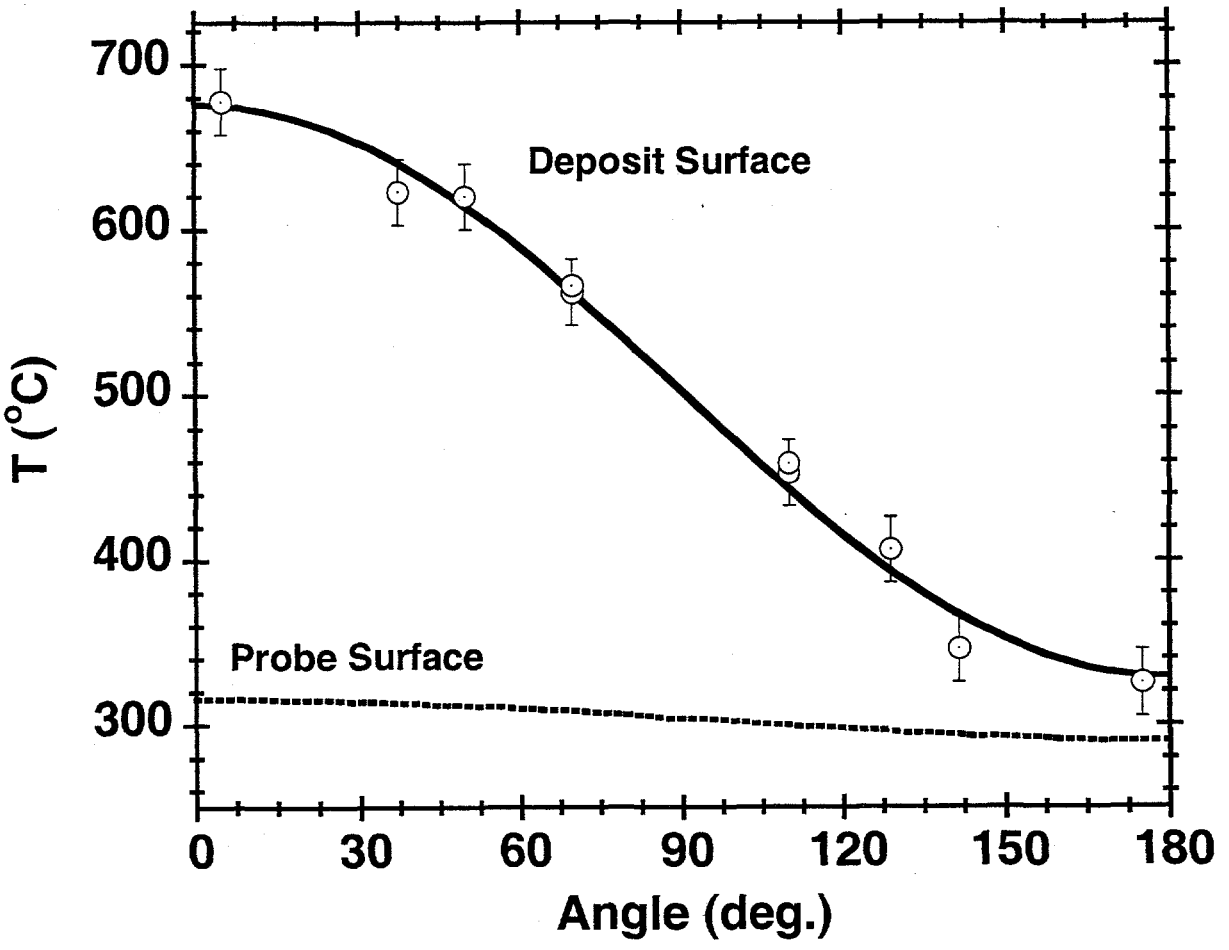


Figure 6 Probe and deposit surface temperature as a function of azimuthal angle θ. The temperature at the leading edge of the probe corresponds to 0°; a plane of symmetry exists along a vertical line drawn between 0° and 180°. The solid line indicates a least-squares fit ($r^2 = 0.98$) of a sinusoid to the average deposit surface temperature measurements made at each angular orientation, which are indicated by the open circles. The vertical bars indicate the uncertainty on deposit surface temperature measurement.

experiments conducted under the same experimental conditions are also presented to illustrate the repeatability of the measurements. These conditions create highly porous, loose, unsintered deposits that can be easily blown or knocked of the deposition probe. The measured solid fraction of all of these deposits is 0.07. In the second part of this study[15], we examine the effects of sintering and deposit microstructure on deposit thermal conductivity.

Theoretical bounds for the thermal conductivity of porous materials provide useful reference points for the evaluation of the measurements; such bounds are discussed in detail in the second part of this study[15]. In Figure 7, we compare our measured values to the simplest, lowest-order bounds, which are defined based on the deposit solid fraction and the thermal conductivity of the gas and solid phases[19]. Treating the gas and solid phases as if they independently conduct heat in series and in parallel defines a lower and upper limit for the effective thermal conductivity, respectively. The thermal conductivity measurements shown in Figure 7 fall between these bounds. To evaluate the

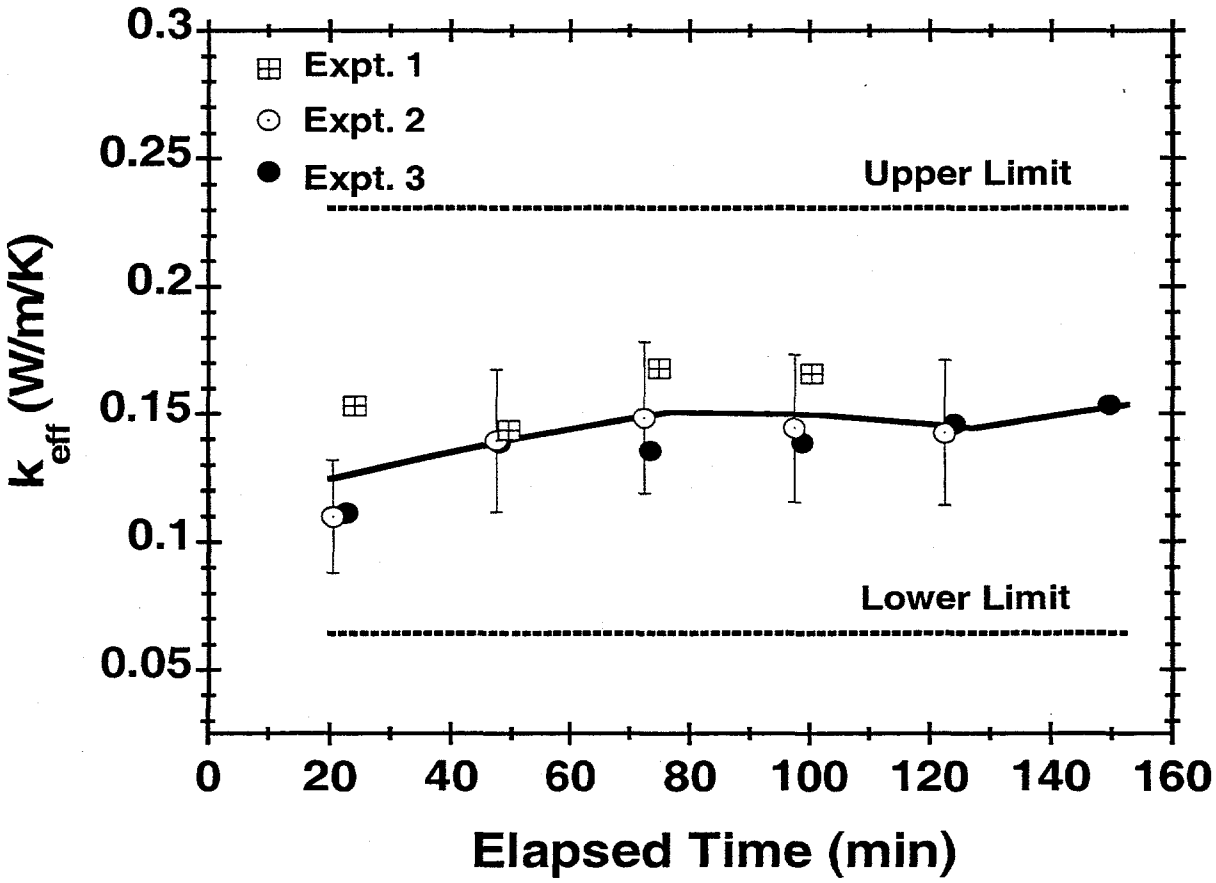


Figure 7 Time-resolved measurements of the thermal conductivity of several deposits formed while firing a 65/35% (by mass) blend of Illinois #6 coal and wheat straw. The measurements indicated by the open circles correspond to the data presented in Figures 3-6. The vertical error bars indicate the maximum experimental uncertainty of ± 20%, and are only shown one set of experimental data for visual clarity.

bounds, we use the measured solid fraction, a value of 0.06 W/(m K) for the thermal conductivity of the gas phase and a value of 3.0 W/(m K) for the thermal conductivity of the solid phase. These values are representative of air and silica-containing materials (the major component of the solid phase) at high temperature[15]. The average measured thermal conductivity, ~ 0.14 W/(m K), shown in Figure 7 is significantly greater than the lower bound, 0.065 W/(m K). Because these deposits are loose and unsintered, we expect that the measured thermal conductivity represents the lower extreme of the range of possible deposits that might form in real boilers. Consequently, it is unlikely that the structure of a real deposit would be such that its effective thermal conductivity is less than air, as has been suggested by some previous work[8,9].

**Experimental Uncertainty**

Comparing the results from several identical experiments, such as those shown in Figure 7, provides an estimate of the repeatability or precision of the experiment. These experiments all produced highly porous deposits with approximately the same solid fraction, 0.07, while firing the same coal-straw blend under the same experimental conditions. The average value of the thermal conductivity from these measurements is 0.14 W/(m K) with a standard deviation of 0.016 W/(m K), and a coefficient of variation (relative uncertainty) of 11%.

The uncertainties of the underlying measurements used to determine deposit thermal conductivity are listed in Table 1. These values are determined from the published manufacturer performance data for each instrument; results from repeated instrument calibration; and analysis of data from the thermal conductivity experiments. The uncertainty of the thermocouple and cooling air flow rate measurements are the manufacturer supplied values verified by repeated calibrations. The uncertainties of the deposit thickness and optical pyrometer measurements are determined by analyzing actual experimental data. The ± 20°C uncertainty listed for the optical pyrometers is the standard deviation of the measured temperature signal when the pyrometer is focused at one location relative to the probe leading edge. This value is significantly greater than the ± 1°C uncertainty that can be achieved when operating the pyrometers under ideal conditions; but is much smaller than the approximately 200°C average temperature difference across the deposit. The larger uncertainty is largely due to roughness of the deposit surface. The ± 40 μm uncertainty in the deposit thickness measurements is the standard deviation of a thickness scan made on a clean probe while feeding solid fuel into the reactor (data from such a scan are labeled 0 min in Figure 4). This

value is significantly larger than the ± 2 μm uncertainty that can be achieved when operating the range finding laser under ideal conditions, but significantly smaller than the overall deposit thickness. The larger uncertainty arises from beam steering in the hot post-combustion gases, particles (fly ash and occasionally burning char) passing through the beam path of the scanning laser, and thermal expansion of the probe as its temperature changes.

Violation of one of the fundamental assumptions underlying the experimental technique represents the final, and potentially most significant, source of experimental error[20]. For our analysis, we neglect axial heat transfer through the deposit. This assumption is not a significant source of uncertainty because the deposit has a small cross-sectional area and a low thermal conductivity; therefore, a large temperature gradient (greater than 50°C/mm) is required to create enough axial heat flux to bias the measurements. Measurements of the axial temperature profile of the deposit surface made by periodically repositioning the pyrometers indicate that there is no significant axial temperature gradient along the deposit surface.

Table 1. Measurement uncertainties.

| Instrument | Uncertainty |
|---|---|
| Probe Thermocouples | ± 5 °C |
| Optical Pyrometers | ± 20 °C |
| Cooling air flowrate | ± 0.5 lpm |
| Deposit thickness | ± 40 μm |

The assumptions underlying our measurement of the heat transfer rate through the deposit are potentially the most significant source of experimental uncertainty. The experiment assumes that within the deposit test section the heat transfer rate through the deposit in the radial direction is equal to the heat transfer rate to the cooling air. This assumption requires that there be no significant axial heat transfer out of the deposit test section. As previously discussed, axial heat transfer through the deposit is negligible. However, axial heat conduction along the stainless steel deposition probe is a significant concern because the high thermal conductivity of stainless steel enables small temperature gradients to drive significant heat transfer. We estimate the potential error due to axial heat transfer along the deposition probe from the measurements of the axial probe surface temperature profile shown in Figure 8a, and the axial probe surface temperature gradient

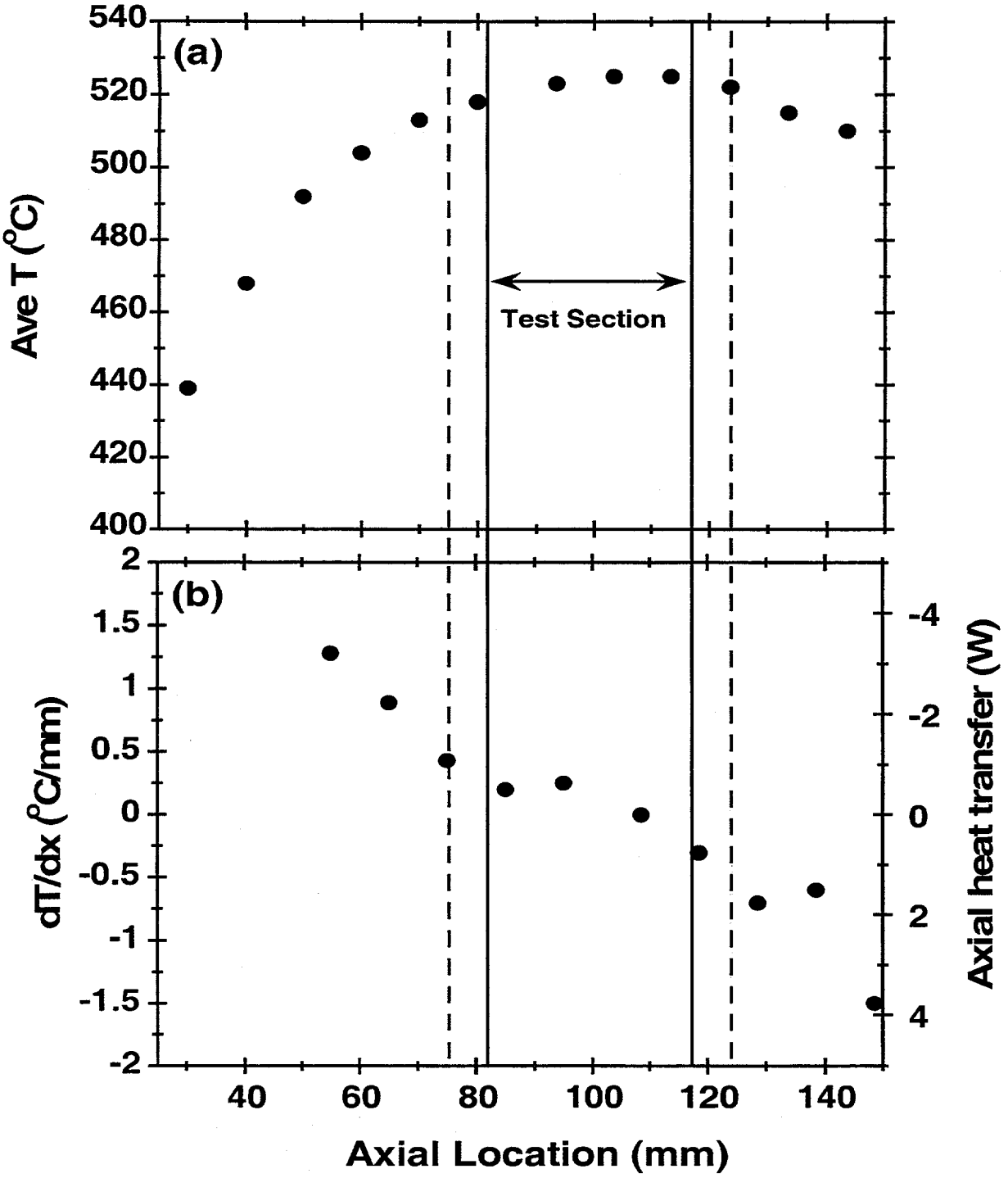


Figure 8 a) Average probe surface temperature, and b) probe surface temperature gradient as a function of axial distance. The vertical dashed lines indicate the 50-mm-wide temperature window and the vertical solid lines indicate the optimum placement of the 35-mm-wide deposit test section within this window. The edges of the reactor tube correspond to 0 and 150 mm. The direction of cooling air flow is from left to right in this figure.

shown in Figure 8b. We calculate the axial heat transfer rate from the calculated axial temperature gradient, the cross-sectional area of the stainless steel wall of the deposition probe (1.14 $cm^2$), and the thermal conductivity of stainless steel (22 W/(m K) at 800 K).

Figure 8a shows that the deposition probe has an asymmetrical axial temperature profile with a peak temperature occurring at 100 mm, two-thirds of the distance across the 150-mm wide reactor. The profile is asymmetrical because of the cooling airflow through the probe. Centered on the peak temperature is a roughly 50-mm-wide window (see Figure 8) in which the error associated with the axial heat transfer is acceptably small—the axial heat transfer rate is less than 1.25 watts. A worst case estimate of the magnitude of this error can be made by assuming a maximum axial heat transfer rate of 1.25 watts out of each end of the test section and using 20 watts as a typical value of the measured heat transfer rate through the deposit (see Figure 3c). Under these worst case conditions, experimental error due to axial heat conduction along the deposition probe is 11%. Optimal placement of the 35-mm-wide deposit test section in 50-mm-wide window reduces this error to about 5%. We use the worst case 11% error in our overall uncertainty analysis.

To ensure that significant axial temperature gradients do not exist within the probe during an experiment, we continuously monitor the axial probe surface temperature profile. (The probe surface temperature thermocouples are axially distributed across the test section for this purpose.) If the temperature difference between any of these thermocouples is greater than 5°C the experiment is terminated.

Combining in quadrature the uncertainty of the individual measurements (± 12%), the estimate of the experimental bias (± 11%), and the precision of the measurements (± 11%), we estimate that the maximum overall relative uncertainty of the thermal conductivity measurements to be ± 20%. An uncertainty of this magnitude is indicated by the vertical error bars shown in Figure 7. A typical relative uncertainty, estimated from typical instead of worst case values, is approximately ± 15%. Although the uncertainty associated with this experimental technique is larger than can be achieved by more traditional techniques for measuring thermal conductivity, we are confident that the approach described in this paper clearly provides more accurate measurements of actual deposit thermal conductivity because of the importance of microstructure in determining deposit thermal conductivity.

## Conclusions

This paper documents a novel experimental design that provides *in situ*, real-time characterization of deposit thermal conductivity under conditions that closely replicate commercial boiler operation. The experiment was designed to minimize the disturbance of the natural deposit microstructure, while providing acceptable levels of experimental uncertainty. We have carefully examined potential sources of error and quantified the overall experimental uncertainty.

For the loose, unsintered deposits considered in this study, the average measured thermal conductivity of $6.14 \pm 0.03$ W/(m K) lags between rational theoretical bounds. We expect that these unsintered and highly porous deposits are representative of the least conductive deposits that might form in real boilers. We believe that these are the first *in situ* or real-time data of this type. The measurement technique does not significantly disturb the natural microstructure of the deposit. This capability is a significant improvement over previous experimental approaches because the thermal conductivity of ash deposits is thought to be largely determined by deposit structure. In the second part of this study[15], this technique is used to examine the impact of densification and sintering on deposit thermal conductivity.

## Acknowledgements

This work was sponsored by the U.S. DOE FETC, Advanced Research and Technology Development Coal Utilization Program. A.L. Robinson was also supported in part by an appointment to the U.S. Department of Energy Fossil Energy Research Participation Program at the Federal Energy Technology Center in Pittsburgh, Pennsylvania, administered by the Oak Ridge Institute for Science and Education.

## References

(1) Couch, G. "Understanding slagging and fouling in pf combustion," IEA Coal Research, 1994.

(2) Baxter, L. L. *Biomass and Bioenergy* **1993**, *4*, 85-102.

(3) Wall, T. F.; Bhattacharya, S. P.; Zhang, D. K.; Gupta, R. P.; He, X. *Progress in Energy and Combustion Science* **1993**, *19*, 487-504.

(4) Wall, T. F.; Bhattacharya, S. P.; Baxter, L. L.; Richards, G.; Harb, J. N. *Fuel Processing Technology* **1995**, *44*, 143-153.

(5) Gupta, R. P.; Wall, T. F.; Baxter, L. L. *The thermal conductivity of ash deposits: Particulate and slag structures*; Gupta, R. P.; Wall, T. F.; Baxter, L. L., Ed.; Engineering Foundation: Kona HI, 1997.

(6) Abryutin, A. A.; Karasina, E. S. *Teploenergetika (Thermal Engineering)* **1970**, *17*, 46-50.

(7) Anderson, D. W.; Viskanta, R.; Incropera, F. P. *Transactions of the ASME Journal of Engineering for Gas Turbines and Power* **1987**, *109*, 215-221.

(8) Boow, J.; Goard, P. R. C. *Journal of the Institute of Fuel* **1969**, *42*, 412-419.

(9) Golovin, V. N. *Teploenergetika (Thermal Engineering)* **1964**, *11*, 23-28.

(10) Mulcahy, M. F. R.; Boow, J.; Goard, P. R. C. *Journal of the Institute of Fuel* **1966**, *39*, 385-394.

(11) Mills, K. C.; Rhine, J. M. *Fuel* **1989**, *68*, 904-910.

(12) Robinson, A. L.; Buckley, S. G.; Baxter, L. L. *In situ measurements of the thermal condcutivity of ash deposits*; Robinson, A. L.; Buckley, S. G.; Baxter, L. L., Ed.; Combustion Institute, Pittsburgh, PA, 1998; Vol. 2, pp 1727-1735.

(13) Belov, S. Y.; Vasil'ev, V. V.; Kovalevich, I. A.; Teterina, T. M. *Teploenergetika (Thermal Engineering)* **1993**, *40*, 692- 694.

(14) Baxter, L. L. *Fuel Processing Technology* **1998**, *56*, 81-88.

(15) Robinson, A. L.; Buckley, S. G.; Yang, N.; Baxter, L. L. *Submitted to Energy & Fuels* **2000**.

(16) Baxter, L. L.; Mitchell, R. E. *Combustion and Flame* **1992**, *88*, 1-14.

(17) Robinson, A. L.; Junker, H.; Buckley, S. G.; Sclippa, G.; Baxter, L. L. *Interactions between Coal and Biomass when Cofiring*; Robinson, A. L.; Junker, H.; Buckley, S. G.; Sclippa, G.; Baxter, L. L., Ed.; Combustion Institute: Boulder, CO, 1998, pp 1351-1359.

(18) Sunden, B. *International Journal of Heat and Mass Transfer* **1980**, *23*, 1359-1367.

(19) Torquato, S. *Applied Mechanics Review* **1991**, *44*, 37-76.

(20) Laubitz, M. J. *Measurement of the thermal conductivity of solids at high temperatures by using steady-state and quasi-linear heat flow*; Laubitz, M. J., Ed.; Academic Press: New York, 1969; Vol. 1, pp 111-183.

**DISTRIBUTION:**

Dr. Donald Aitken
Union of Concerned Scientists
2625 Alcatraz Ave., Suite 505
Berkeley, CA 94705

Dr. Suresh P. Babu
Institute of Gas Technology
1700 South Mount Prospect Road
DES PLAINES, Illinois 60018-1804

Mr. Phillip Badger
Tennessee Valley Authority
SE Regional Biomass Program
PO Box 1010
Muscle Shoals, AL 35662-1010

Dr. Richard Bain, Manager
Biomass Power Program
National Renewable Energy Laboratory
1617 Cole Boulevard
Golden, Colorado 80401-3393

Dr. Steve Benson
UND Energy and Environ. Res. Center
P.O. Box 9018
Grand Forks, ND 58202-9018

Mr. William M. Burnett
Senior Vice President
Technology Development
Gas Research Institute
8600 West Bryn Mawr Avenue
Chicago, IL 60631

Mr. William H. Carlson
Wheelabrator Environmental Systems
20811 Industry Road
Anderson, CA 96007

Mr. Kevin Craig
Biomass Power Program
National Renewable Energy Laboratory
1617 Cole Boulevard
Golden, Colorado 80401-3393

Dr. Raymond Costello
Manager
Biomass Power Program, EE-13
U.S. DOE
1000 Independence Avenue, SW
Washington, D.C. 20585

Dr. Stefan Czernik
Research Chemist
National Renewable Energy Laboratory
1617 Cole Boulevard
Golden, Colorado 80401-3393

Professor John W. Daily
Univ. of Colorado at Boulder
Mechanical Engineering Dept.
Boulder, CO 80309-0427

Dr. Kevin Davis
Reaction Engineering International
77 West 200 South, Suite 210
Salt Lake City, UT 84101

Dr. David Dayton
Staff Thermochemical Scientist
National Renewable Energy Laboratory
1617 Cole Boulevard
Golden, Colorado 80401-3393

Dr. Thomas H. Dunning, Jr., Manager
Molecular Sciences Research Center
Pacific Northwest National Laboratories
P. O. Box 999, MS K2-20
Richland, WA 99352

Prof. Christopher F. Edwards
Dept. of Mechanical Engineering
Stanford University
Stanford, CA 94305-3032

Dr. Robert Evans
National Renewable Energy Laboratory
1617 Cole Boulevard
Golden, Colorado 80401-3393

**DISTRIBUTION: (continued)**

Dr. Robert B. Finkelman
U.S. Geological Survey
956 National Center
Reston, VA 22092.000

Prof. Rick Flagan
California Institute of Technology
Environmental Engineering Dept.
Mailcode 138-78
Pasadena, CA 91125

Prof. Thomas Fletcher
Department of Chemical Engineering 350
Clyde Building
Brigham Young University
Provo, UT 84602

Dr. Patrick F. Flynn
Vice President, Research & Technology
Cummins Engine Company
Mail Code 50181, Box 3005
Columbus, IN 47202-3005

Dr. W. James Frederick Jr.
Institute of Paper Science And Technology
500 - 10th Street NW
Atlanta, GA 30318

Ms. Alia Ghandour
Director of International Programs
National BioEnergy Industries
Association (NBIA)
1212 C St. NW, 4th Floor
Washington, DC 20001-2109

Mr. Philip Goldberg
US DOE / NETL
922-342
626 Cochran Mill Road
P.O. Box 10940
Pittsburgh, PA 15236-0940

Dr. J. Peter Gorog
Research and Development
Pulp, Paper and Packaging
Weyerhaeuser Company
WTC 2H22
Tacoma, WA 98477

Mr. Jeff Graef
W Regional Biomass Energy Program
Nebraska Energy Office
1200 N Street Suite 110
Lincoln, NE 68509-5085

Mr. Richard Handley
NE Regional Biomass Energy Program
Coneg Policy Research Center Inc.
400 N Capital St NW Suite 382
Washington, DC 20001

Professor Ronald K. Hanson, Chair
Department of Mechanical Engineering
Stanford University
Stanford, CA 94305

Dr. Mike Heap
Reaction Engineering International
77 West 200 South_Suite 210
Salt Lake City, UT 84101

Dr. Evan Hughes
Manager, Renewable Fuels
Electric Power Research Institute
3412 Hillview Avenue
P.O. Box 10412
Palo Alto, CA 94303

Prof. Robert Hurt
Division of Engineering
Brown University
Box D
Providence, RI 02912

**DISTRIBUTION: (continued)**

Dr. Ari Huttunen
EPRI
Coal Combustion & Renewables
Energy Conversion
3412 Hillview Ave.
Palo Alto, CA 94304-1395

Professor Bryan M Jenkins
University of California, Davis
Biological and Ag. Eng. Dpt.
Davis, CA 95616-5294

Dr. Andrew K. Jones
International Paper
Manufacturing Technology Center
6285 Tri-Ridge Blvd.
Loveland, OH 45140-7910

Mr. Frederick Kuzel
Council Great Lakes Governors
Great Lakes Regional Biomass Program
35 E Wacker Drive Suite 1850
Chicago, IL 60601

Dr. Steve Londerville
Director of Research & Development
The Coen Company, Inc.
1510 Rollins Road
Burlingame, CA 94010

Professor Gregory J. McRae
Department of Chemical Engineering
Massachusetts Institute of Technology
Room 66-372
77 Massachusetts Avenue
Cambridge, MA 02139-4307

Dr. Arun Mehta
Electric Power Research Institute
3412 Hillview Avenue
Palo Alto, CA 94304-1395

Mr. Thomas R. Miles
Consulting Design Engineer
5475 SW Arrowwood Lane
Portland, OR 97225

Professor Reginald E. Mitchell
Dept. of Mechanical Engineering
Stanford University
HTGL 520C,
Stanford, CA 94305-3032

Dr. Gregory P. Morris
Future Resources Associates, Inc.
2039 Shatuck Ave. Suite 402
Berkeley, CA 94704

Dr. Ralph P. Overend
National Renewable Energy Lab
1617 Cole Boulevard
Golden, CO 80401-3393

Mr. Pekka Pakkala
Embassy of Finland
Technology Center
3301 Massachusetts Ave., NW
Washington, DC 20008

Prof. David Pershing
University of Utah
2202 MEB
Salt Lake City, UT 84112

Dr. Thomas Reed
Colorado School of Mines
1810 Smith Road
Golden, CO 80401

Ms. Valri Robinson
Office of Industrial Technologies
DOE, EE-22, Room 5F-035
Washington D.C. 20585

**DISTRIBUTION: (continued)**

Mr. Robert Roscoe
Weyerhaeuser
Technology Center
Federal Way, WA 98003

Prof. Daniel E. Rosner
Yale University
Mason Laboratory
New Haven, CT 6520

Prof. Adel Sarofim
Univ. of Utah & MIT
Dept. of Chemical Eng.
Salt Lake City, UT 84112

Dr. Daniel J. Seery
Senior Program Manager
Environmental Science
United Technologies Research Center
East Hartford, CT 06108

Dr. David G. Sloan
ABB-Combustion Engineering, Inc.
2000 Day Hill Road
Windsor, CT 6095

Prof. Philip Smith
Dept. of Chemical and Fuels Engineering
2250 Merrill Engineering Building
Salt Lake City, UT 84112

Prof. L. Douglas Smoot
Department of Chemical Engineering
435T Crabtree Technology Building
Brigham Young University
Provo, Utah 84602

Mr. Scott M. Smouse
NETL
P.O. Box 10940
Pittsburgh, PA 15236-0940

Dr. Peter Solomon
Advanced Fuel Research
P.O. Box 18343
East Hartford, CT 6108

Dr. John Stringer
Executive Technical Fellow
Electric Power Research Institute
3412 Hillview Avenue
Palo Alto, CA 94303

Dr. David A.Tillman
Foster Wheeler Development Corporation
Perryville Corporate Park
Clinton, NJ 08809-4000

Dr. Chris Verrill
Research Chemical Engineer
Westvaco Corporation
PO Box 118005
Charleston, SC 29423-8005

Mr. Dave Waltzman
US Department of Energy
Denver Regional Support Office
1617 Cole Boulevard
Golden, CO 80401

Mr. Larry Watson
Chevron Research & Technology
100 Chevron Way
Richmond, CA 94802

Prof. Jost O. L. Wendt
Dept. of Chemical Engineering
University of Arizona
Tucson, AZ 85721

Dr. Rick Wessel
McDermott Technologies Inc.
1562 Beeson St.
Alliance, OH 44601

**DISTRIBUTION: (continued)**

Prof. Judy Wornat
Dept. of Mech. & Aerospace Engr.
Princeton University
Princeton, NJ 08544-5263

Mr. Warren Zurn
DOE Atlanta Support Office
730 Peachtree Street NE Suite 876
Atlanta, GA 30308

Dr. Franscisco Domingues Alves de Sousa
Instituto de Pesquisas Tecnologicas do
Estado de Sao Paulo - IPT
Cidade Universitaria - CEP 05508-901
Sao Paulo-SP, Brazil

Dr. Javier Ballester
University of Zaragoza
María Zayas, 12, 5° A
50015-Zaragoza
Spain

Professor Tony Bridgwater
Chem. Eng. And Appl. Chem.
Aston University
Aston Triangle
Birmingham B4 7ET
United Kingdom

Dr. Mark Douglas
A/Group Leader, CO2 Abatement
CANMET Energy Technology Center
1 Haanel Drive
Nepean, ON K1A 1M1
Canada

Professor Kim Dam-Johansen
Hempel's Marine Paints A/S
Lundtoftevej 150
DK-2800 Lyngby
Denmark

Mr. John Gifford
Project Leader, Energy
Forest Research
Private Bag 3020
Rotorua
New Zealand

Dr. Alexandre J. Grebenkov
Head of Laboratory
Institute of Power Engineering Problems
Sonsy, 220109
Minsk
Belarus

Dr. Steven Gust
Fortum
Technology Centre
P.O. Box 310
FIN-06101
Porvoo, Finland

Prof. Klaus R. G. Hein
Universität Stuttgart
Pfaffenwaldring 23
7000 Stuttgart 80
GERMANY

Prof. Hermann Hofbauer
Institut fur Verfahrenstechnik
Brennstofftechnik und Umwelttechnik
Getreidmarkt 9
A-1060 Wien
Austria

Dr. Patrick Hughes
Natural Resources – Canada
CANMET
1 Haanel Drive
Nepean, Ontario
Canada K1A-1M1

**DISTRIBUTION: (continued)**

Prof. Mikko Hupa
Åbo Akademi University
Lemminkäisenkatu 14-18 B
FIN-20520 Åbo/Turku
Finland

Prof. Johan Hustad
SINTEF Thermal Energy and
Fluid Machinery
7034 Trondheim
Norway

Dr. Jun Inumaru
Central Research Institute
of Elec. Power Ind.
2-6-1 Nagasaka, YOKOSUKA 240-01
Japan

Dr. Tommy Jacobon
Fortum Power and Heat Oy
POB 20, 00048
FORTUM, Finland

Mr. Henrik Houmann Jakobsen
DK-Teknik
Gladsaxe Mollevej 15
DK-2860 Soborg
Denmark

Mr. Kauko Janka
Kværner Pulping Oy
Kelloportinkatu 1 D
Box 109
Tampere, FIN+33101
Finland

Dr. Helle Junker
Elsamprojekt A/S Power Station
Engineering
53 Kraftvaerksvej
DK-7000 Fredericia
Denmark

Dr. Jaap Koppejan
TNO Institute of Environmental Sciences
Dept. of Thermal Conversion Technology
P.O. Box 342
7300 AH Apeldoorn
The Netherlands

Dr. Alexander A. Mikhalevich
Academy of Sciences, Belarus
Institute of Power Engineeing Problems
IPEP, SOSNY
Russia

Dr. Thomas Nussbaumer
Verenum
Langmauerstrasse 109
CH-8006 Zurich
Switzerland

Dr. Ingwald Obernberger
Institute of Chemical Engineering
Technical University of Graz
Inffeldgasse 25
A-8010 Graz
Austria

Dr. Aksel Olsen
Risoe National Laboratory
Optics & Fluid Dynamics Dept.
P.O. Box 49 – Bldg. OFD-201
Frederiksborgvej 399
DK-400 Roskilde
Denmark

Mr. Heikki Oravainen
VTT Energy
Fuels and Combustion
P.O. Box 1603
FIN-40101-Jyvaskyla
Finland

**DISTRIBUTION: (continued)**

Dr. Niranjan Patel
ETSU, B156
Harwell
OXON OX11 0RA
UNITED KINGDOM

Prof. Dimos Poulikakos
Swiss Federal Institute of Technology
Institute for Energy Technology
ETH-Zentrum
CH-8092 Zürich
Switzerland

Mr. Erik Rensfelt
TPS Termiska Processer AB
Studsvik S-611 82 Nykoping
Sweden

Mr. Joe Robert
CANMET
580 Booth Street-13th Floor
Ottavwa, Ontario K1A 0E4
Canada

Dr. Yves Schenkel
Chef de travaux-Section Biomass
Head-Biomass Unit
CRA-Departement Genie rural
Chee de Namur, 146
B-5030 Gembloux
Belgium

Dr. Oyvind Skreiberg
Institutt for Termisk Energi og Vannkraft
Fakultet for Maskinteknikk
NTNU, 7491 Trondeim
Norway

Dr. Yrjo Solantausta
VTT Energy
PO Box 1610
FIN-0244 VTT, ESPOO
Finland

Mr. Frans Sulilatu
TNO-MEP, Dep. Combustion Conversion
P.O. Box 342
NL-7300 AH Apeldorn
Netherlands

Dr. Raj Thamburaj
Director, Research and Development
Orenda Aerospace Corporation
3160 Derry Road East
Mississauga, Ontario L4T 1A9
Canada

Professor Honghi Tran
Department of Chemical Engieering &
Applied Chemistry
University of Toronto
200 College Street
Toronto, Canada M4S 1A4

Mr. John Tustin
Forest Research
Private Bag 3020
Rotorua
New Zealand

Mr. Sjaak van Loo
TNO, PO Box 342
NL-7300 AH Apeldoorn
The Netherlands

Prof. Terry Wall
University of Newcastle
Rankin Drive
Newcastle 2308
NSW
Australia

Prof. Franz Winter
Technische Universität Wien
Institut Fuer Verfahrenstechnik
A-1060 Wien
Austria

**DISTRIBUTION: (continued)**

MS0750 D. J. Borns, 6116

MS0741 S. G. Varnado, 6200

MS0703 T. R. Mancini, 6216

MS9001 M.E. John, 8000
Attn: 8100 J. Vitko
8400 D. Hensen
8700 M. Dyer
8900 K. Washington

MS9105 B. Wu, 8119

MS9054 W. J. McLean, 8300
Attn: 8350 F. Tully
8351 L. Rahn
8356 R. Gallagher
8360 R. Carling
8362 J. Keller
8901 T. Bramlette

MS9052 L. L. Baxter, 8361 (10)

MS9052 D. R. Hardesty, 8361(13)

MS9052 T. Lind. 8361

MS9052 G. Sclippa, 8361

MS9052 C. R. Shaddix, 8361

MS9051 A. E. Lutz, 8362

MS9053 P. Walsh, 8366

MS9403 J. Wang, 8723
Attn: N. Yang

MS9042 M. Perra, 8728
Attn: S. Griffiths
W. Houf
R. Larson
R. Nilson

MS9018 Central Technical Files, 8940-2 (3)

MS0899 Technical Library, 4916

MS9021 Technical Communications Department, 8528/Technical Library, MS 0899, 4916

MS9021 Technical Communications Department, 8528 for DOE/OSTI

MS 0161 Patent and Licensing Office, 11500